Eng. Sci., 2025, **37**, 1804

Engineered Science
DOI: https://dx.doi.org/10.30919/es1804

MXene-Integrated Porous Carbon–Silicon Composite as a Stable and High-Capacity Anode for Lithium-Ion Batteries

Nadira Saitova,[1,2] Kydyr Askaruly,[1,2,4,*] Nurlan Idrissov,[1,3] Zhanserik Kuli,[1] Kalizhan Shakenov,[1,*] Seitkhan Azat[1] and Shynggyskhan Sultakhan[1]

Abstract

In this work, a novel composite anode material combining activated carbon, MXene, and nanosized silicon was developed for high-performance lithium-ion batteries. Unlike previously known MXene/Si or Si/C systems, our work is the first to implement a three-component AC/Si/MXene architecture, where biomass activated carbon provides a highly developed porous structure and additional conductivity, MXene stabilizes and enhances electron transport, and nano-Si contributes high capacitance. The composite design integrates the advantages of each component: silicon for its high theoretical capacity, MXene for its excellent electrical conductivity and layered structure, and biomass-derived activated carbon for its high surface area and structural integrity. A sequential synthesis strategy was employed, where nanosilicon was first intercalated into MXene layers, followed by mixing with porous activated carbon to form a homogeneous and stable hybrid structure. Here, the synthesized MXene material acts as a matrix for nanosilicon to restrain volume expansion during charge/discharge, and the synthesized activated carbon acts as a conductor for structural stability and also has additional capacity. Electrochemical analysis of the AC/Si/MXene composite demonstrated a high initial discharge capacity exceeding 2000 mAh/g at a current density of 200 mA/g. Subsequent capacity studies at different current densities showed that the material is stable. The composite material also showed higher capacity compared to individual nano-Si, MXene, and AC.

Keywords: Activated carbon; Mxene; Energy storage; Composite; Lithium-ion battery.
Received: 09 September 2025; Revised: 23 September 2025; Accepted: 07 October 2025
Type: Research article.

1. Introduction

Lithium-ion batteries are currently the leading energy storage technology among electrochemical power sources. Since their commercialization, they have caused a real revolution in the field of portable electronics and, subsequently, in electric vehicles and the energy sector.[1] Currently, most existing electric vehicles are equipped with lithium-ion batteries due to their high specific energy, long cycle life and satisfactory efficiency. However, with the increasing demand for lithium and the limited its limited natural availability, as well as the high cost and potential risks associated with thermal instability, intensive research is underway to develop alternative energy storage systems.[2] Promising candidates include sodium-ion batteries,[3] flow batteries,[4] as well as alkaline and other types of rechargeable batteries.[5,6] However, despite ongoing efforts to find alternatives, lithium-ion technology remains the most widely used and commercially mature energy storage system today.[7]

Since the advent of lithium-ion batteries, carbon, primarily in the form of graphite, as the anode material of choice.[8] This material has proven to be a stable and efficient host for lithium ions due to its high reversible capacity, excellent cycling stability, and wide availability. In the early stages of lithium-ion battery development, graphite fully met the performance requirements of anode materials. However, as the use of lithium-ion batteries has expanded especially in large-scale energy storage systems and electric vehicles the energy characteristics of graphite have increasingly become a limiting factor. Despite the theoretical specific capacity of 372 mAh/g, in practice graphite anodes usually reach only 280-310 mAh/g.[9] Commercial cells also use alternative anode materials such as lithium titanate (LTO) and other oxide-based structures, including spinels.[10] Although their specific capacity is lower than that of graphite, they provide high charge-discharge rates and increased stability, making them preferred for applications requiring high power density and long cycle life.

Intensive research is currently underway to replace graphite with higher-capacity materials.[11] One of the most

---

[1] *Satbayev University, 22 Satbaev Street, Almaty, 050000, Kazakhstan*
[2] *Bes Saiman Group, 38 Tulebaev Street, Almaty, 050057, Kazakhstan*

promising candidates is silicon, which has a theoretical specific capacity of about 4,200 mAh/g, which is almost ten times that of graphite. This exceptional capacity makes silicon a very attractive material for the development of next-generation anodes for lithium-ion batteries.[12] Despite its high theoretical specific capacity, the widespread use of silicon in lithium-ion batteries is still limited by several significant disadvantages. The main problem lies in the significant volume changes that silicon undergoes during lithiation and delithiation.[13] When reacting with lithium ions, silicon forms the intermetallic compound $Li_{4.4}Si$, accompanied by a volumetric expansion of up to 300%.[14] Such a significant volume expansion leads to mechanical stresses, cracking, and structural degradation of silicon during cycling. As a result, the electrical connection between the active particles is disrupted, forming inactive ("dead") areas, which leads to a sharp decrease in capacity and worsens the stability of the cycle. To mitigate these disadvantages, researchers are developing silicon-based composite materials using various chemical, physical, and mechanical approaches.[15,16] These methods are aimed at reducing volume changes, increasing conductivity, and stabilizing the structure of the anode material. The most promising strategies include the development of silicon-carbon composites, nanostructuring, silicon encapsulation, and the use of buffer matrices capable of withstanding volumetric expansion.[17]

In recent years, composite materials based on MXene in combination with silicon and carbon have been actively studied.[18] MXene structures (for example, $Ti_3C_2T_x$) exhibit exceptionally high electrical conductivity, significantly exceeding that of traditional carbon materials.[19] This makes them particularly attractive as conductive matrices or buffer phases in anode composites for lithium-ion batteries.

For example, in the work of Huang Liu *et al*.,[20] a composite material based on two-dimensional quantum dots SnO_2 and MXene ($Ti_3C_2T_x$) was synthesized using chemical methods. The resulting material demonstrated a specific capacity of 659.8 mAh/g after 100 cycles, retaining 91% of its original value, which indicates the high stability and efficiency of the composite.[21] For comparison, the pure synthesized MXene in the same study demonstrated a capacity slightly above 100 mAh/g, which is consistent with our experimental results. Several studies have attempted to solve the problems of bulk expansion of silicon and low electrical conductivity by integrating it with MXene materials. For example, in,[22,23] silicon was intercalated between MXene layers, forming multilayer hybrid structures with high electrical conductivity and the ability to effectively buffer volume changes occurring during lithiation and delithiation.

An alternative approach was implemented in the study,[24] where silicon particles were encapsulated within an MXene shell, forming capsule-like structures. This architectural design effectively prevents particle agglomeration and contributes to improved structural stability during cycling. Furthermore, in the study,[25] a composite structure was proposed in which active silicon and MXene were uniformly distributed, ensuring full contact between the components. Such a design enhances both ionic and electronic transport and significantly improves the cycling stability of the material. In addition to silicon, MXene is also actively employed in combination with various forms of activated carbon (AC). For example, the study[26] describes the development of composite materials based on carbon fibers and MXene, which demonstrated high efficiency when applied in electrochemical energy storage devices. In another study,[27] activated carbon in particle form was combined with MXene to fabricate supercapacitor electrodes, resulting in high specific capacitance and excellent cycling stability.

Taking into account the above-mentioned approaches and the results of previous studies, this study proposes the synthesis of a composite anode material including MXene, activated carbon, and nanosilicon. Initially, MXene and porous activated carbon are synthesized, with the latter serving as a conductive and mechanically stable matrix. The nanosilicon was anchored onto the surface and edges of MXene sheets, forming a hybrid MXene/Si structure with close interfacial contact. While full intercalation between the interlayer galleries is unlikely due to the size of the silicon nanoparticles (~tens of nanometers), their uniform distribution across the MXene surface facilitates efficient electronic and ionic transport, and helps to buffer volume expansion during cycling.

2. Experimental section

2.1 Synthesis of activated carbon

Activated carbon was synthesized using a two-step method involving thermal carbonization and chemical activation of apricot kernels shell biomass (ASh). In the first step, 50 g of ASh were washed under running tap water for 30 minutes, followed by three rinses with distilled water to remove surface contaminants, dust, soluble salts, and organic impurities. After filtration and drying at 105 °C for 12 hours, the cleaned raw material was placed into a sealed stainless-steel reaction vessel. Carbonization was carried out under an argon atmosphere (flow rate: 300 mL/min) at a temperature of 550 °C with a heating rate of 6 °C/min and a holding time of 90 minutes. The resulting carbonized product (~20 g) was cooled to room temperature under an inert atmosphere.

For chemical activation, the carbonized ASh was mixed with potassium hydroxide (KOH) at a mass ratio of 1:4 (carbon precursor: KOH). The mixture was thoroughly ground in an agate mortar. Thermal activation was then performed in the same reactor at 800 °C for 120 minutes,

---

[3]*Institute of nuclear physics, 1 Ibragimov Street, Almaty, 050032, Kazakhstan*

[4]*Engineering and Science Hub, 38 Tulebaev Street, Almaty, 050004, Kazakhstan*

[*]*Email:* k.askaruly@gmail.com (K. Askaruly), k.shakenov@satbayev.university (K. Shakenov)

using the same heating rate (6 °C/min) and argon flow (300 mL/min). After cooling, the activated carbon was washed with hot distilled water (70–80 °C) until a neutral pH (~6–7) was reached, confirming the complete removal of residual alkaline activating agents.

Final drying was carried out in an oven at 130 °C for 12 hours. The obtained activated carbon was stored in a sealed glass container until further use (Fig. 1). The final yield of the activated carbon was approximately 34% of the initial mass.

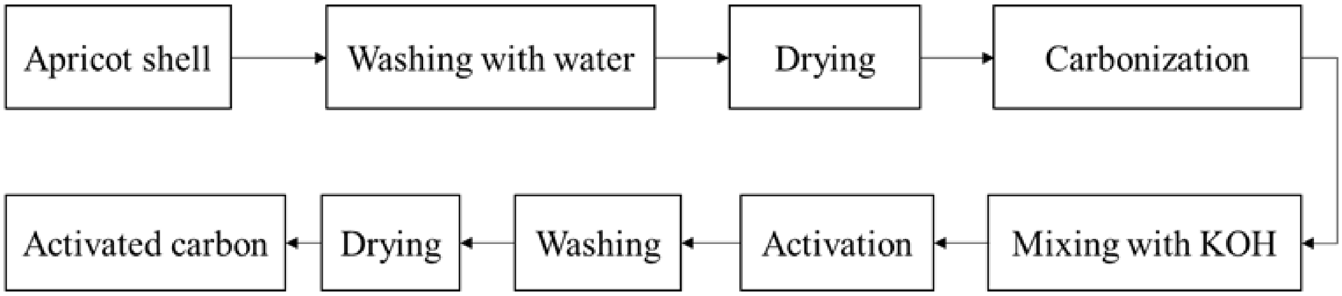

Fig. 1: Schematic diagram of the Step-by-step synthesis of activated carbon from apricot shell.

2.2 Synthesis of MAX Phase and MXene

High-purity powders of titanium (Ti), titanium carbide (TiC), and aluminum (Al) were used for the synthesis of the MAX phase. The components were mixed in pre-calculated molar ratios corresponding to the desired Ti_3AlC_2 composition. The mass of each substance was determined based on its molar mass, and the components were weighed precisely using an analytical balance. The resulting mixtures were subjected to mechanical mixing in a planetary ball mill equipped with an iron container and stainless-steel balls. The milling process was carried out at a rotation speed of 150 rpm for 24 hours. The mass ratio of the powder mixture to the milling balls was 1:3, ensuring effective grinding and homogenization.

The mixed powders were then sintered in a tubular furnace under a high-purity argon atmosphere (99.999%). Prior to sintering, the system was evacuated and purged with argon three times to eliminate residual air. The heating profile involved a temperature ramp of 5 °C/min followed by a 120-minute dwell at the target temperature. The argon flow rate was maintained at 100 mL/min. After heat treatment, the samples were allowed to cool to room temperature inside the furnace to prevent thermal cracking. The sintered samples were then ground into a fine powder using a diamond mill and sieved through a 0.46 µm mesh to obtain a uniform particle distribution.

The synthesized MAX phase powders were subjected to chemical etching using hydrochloric acid (HCl). To prevent a highly exothermic reaction, 1 g of Ti_3AlC_2 powder was slowly added to concentrated HCl. Under continuous stirring with a PTFE-coated magnetic stir bar, 0.666 g of LiF was gradually added to the mixture. The stirring process was continued for 30 minutes to ensure complete dissolution of the salt. The resulting suspension was incubated at 32 °C for 24 hours.

Upon completion of the reaction, the mixture was washed with deionized water or ethanol until a neutral pH (approximately 6) was reached. The washing procedure consisted of several cycles, each involving the addition of deionized water (or ethanol), centrifugation (3500 rpm, 10 minutes), and decanting. Typically, four washing cycles were performed. As a result, a high-purity MXene material was obtained and stored in distilled water for further use (Fig. 2).

2.3 Synthesis of the Composite Material

To prepare the composite material, 10 mg of nanodispersed silicon was dispersed in 10 mL of distilled water using an ultrasonic bath for 30 minutes to ensure uniform particle distribution. Afterward, 10 mL of an aqueous MXene solution was added to the suspension at a 1:1 volume ratio, and the mixture was further stirred mechanically at room temperature until a homogeneous MXene/Si solution was obtained.

The resulting mixture was then introduced into 1 g of pre-prepared activated carbon, followed by vigorous stirring using a magnetic stirrer for 1 hour to promote uniform adsorption and interaction of the components. Upon completion of

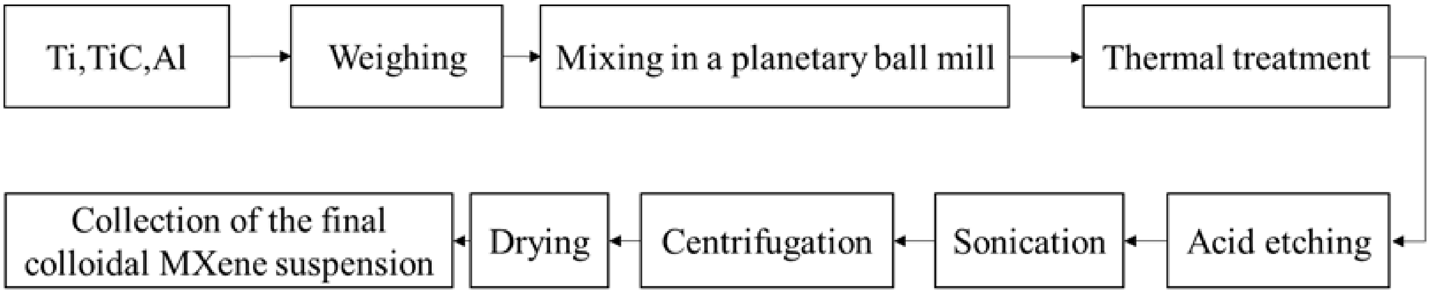

Fig. 2: Step-by-step process of MAX phase synthesis followed by selective etching and delamination to obtain $Ti_3C_2T_x$.

Fig. 3: Step-by-step synthesis of the AC/Si/MXene composite material.

mixing, the resulting composite was dried in a vacuum oven at 120 °C for 12 hours. The dried material was then mechanically ground in a planetary ball mill for 30 minutes to obtain a homogeneous, highly dispersed powder (Fig. 3).

2.4 Electrode Preparation

To fabricate working electrodes, the composite materials were mixed with conductive carbon black (Timical Super C45, Sigma-Aldrich) and polyvinylidene fluoride (PVDF, Arkema HSV900, Sigma-Aldrich) in a mass ratio of 8:1:1. N-methyl-2-pyrrolidone (NMP, Sigma-Aldrich) was used as the solvent. The resulting slurry was mechanically stirred in an agate mortar for 30 minutes until a homogeneous suspension was obtained.

The suspension was applied to stainless steel foil (thickness: 16 µm) using a 100 µm-thick doctor blade. The coated electrodes were dried in a vacuum oven at 120 °C for 12 hours. After drying, circular discs with a diameter of 16 mm were punched from the electrode film. The active material loading was calculated per unit area of each disc to ensure standardized electrochemical measurements (the mass loading of the active material was approximately 3.4 mg per electrode). CR2032-type half-cells were assembled in an argon-filled glove box (with H_2O and O_2 levels below 0.1 ppm) using the prepared electrodes. A 1 M solution of $LiPF_6$ in a 1:1 volume mixture of ethylene carbonate (EC) and dimethyl carbonate (DMC) was used as the electrolyte. Lithium metal foil served as the counter electrode. The assembled cells were used for subsequent electrochemical characterization of the composite materials (Fig. 4).

Fig. 4: Schematic representation of the preparation of electrode and testing.

2.5 Characterization methods

The mineralogical composition of the samples was analyzed by X-ray phase analysis using the MPD XCEL-221 diffraction system at 30 kV and 10 mA, with CuKa radiation. The morphological characteristics surface was studied using scanning electron microscopy (SEM) using a scanning electron microscope, elemental analysis was performed using an energy dispersion spectrometer Si (Li) (Joel JSM-6490 LA) connected to SEM. Nitrogen adsorption at −196 °C using Autosorb-1 (Quantachrome, Hook) performed the pore size distribution and specific surface area analysis. The pore size distribution was calculated using the BJH method, while the specific surface area was determined using the BET method. pH meter (Multiparameter Water Quality Meter). For cell testing, a BTS-5V50mA 8-Channel Coin Cell Battery Voltage Analyzer Tester was used for charge–discharge and stability measurements, while a potentiostat/galvanostat Elins P-40X was employed for impedance spectroscopy and cyclic voltammetry.

3. Results and discussion

One of the main methods of analyzing porous materials is the BET analysis, which determines the specific surface area and gives an idea of the porosity and textural development of the material. Fig. 5 shows the nitrogen adsorption-desorption isotherm at 77 K (left) and the pore size distribution (right) for synthesized activated carbon. The isotherm exhibits a characteristic type IV behavior with an H4 hysteresis loop, which indicates a well-developed micro-mesoporous structure of the material.[28] At low relative pressures ($P/P_0 < 0.1$), a sharp increase in the adsorption volume is observed, which is explained by the filling of micropores with a diameter of less than 2 nm. A further gradual increase in adsorption in the range of $P/P_0 = 0.1–0.4$ corresponds to the filling of mesopores (2-50 nm), typical for activated carbons obtained by chemical activation methods. At $P/p_0 > 0.4$, the isotherm reaches a plateau, which indicates a limited macroporosity.[29]

Analysis of the pore size distribution (Fig. 5a) by the BJH method shows that the predominant pore diameter is in the range of 2-5 nm, which confirms the mesoporous nature of the material with a significant contribu-tion of micropores. The cumulative pore volume curve shows a total pore volume of approximately 1.6 cm^3/g. The specific surface area calculated using the multipoint BET method is 3450.96 m^2/g, which in-dicates a very high degree of activation and effective pore development (Fig. 5b).

Fig. 6 shows images of synthesized MXene ($Ti_3C_2T_x$) in a transmission electron microscope at various magnifications. In the left image (scale ruler: 50 nm), thin layered structures characteristic of MXene are observed, demonstrating a well-defined lamellar morphology, which confirms the successful etching of aluminum from the MAX phase and subsequent stratification. The distinct transparent areas correspond to a single or multi-layered MXene sheet, while the darker areas indicate the stacking of mul-tiple layers. In the right image (scale ruler: 100 nm) shows larger aggregates and fragments of layered structures showing thin lamellar morphology with varying degrees of transparency. This structure provides a

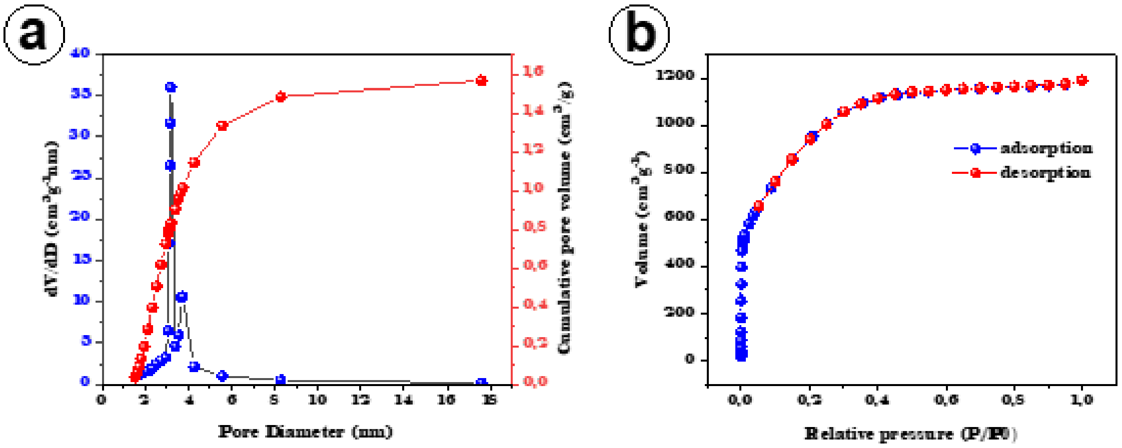

Fig. 5: N2 adsorption/desorption isotherm (a) and pore size distribution curve (b) based on the Brunauer-Emmett-Teller method for the activated carbon.

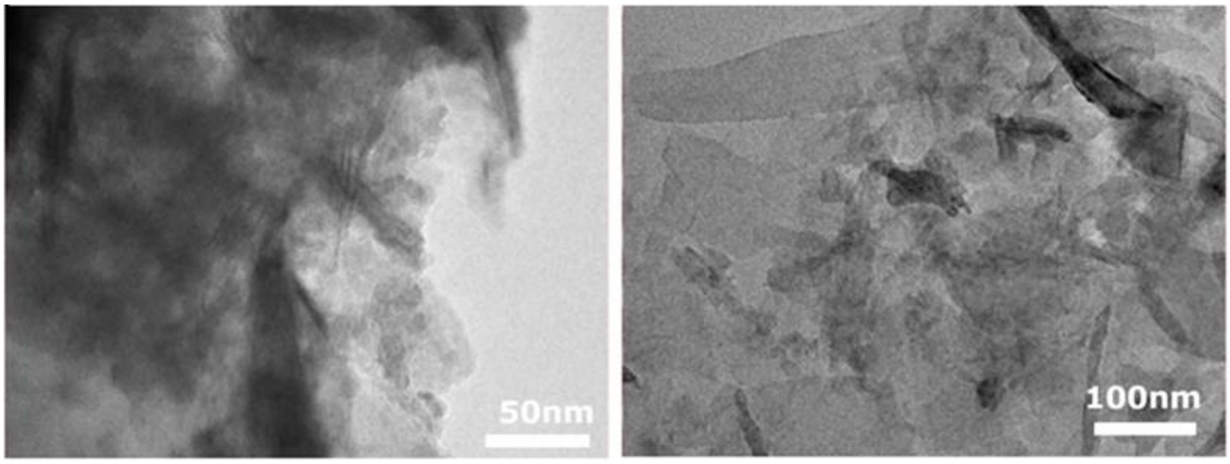

Fig. 6: TEM image of MXene nanosheets at 50-100 nm.

large surface area and accessible active centers, which are crucial for the application of MXene as an electrode material in lithium-ion batteries and supercapacitors.

The TEM results confirm that the synthesized MXene exhibits a typical multilayer two-dimensional structure with a high degree of stratification, which provides effective interlayer interaction and excellent electrical conductivity. Scanning electron microscopy (SEM) analysis was performed to assess the morphology and surface structure of intermediate and composite samples, as shown in Fig. 7. Comparative image analysis allows microstructural changes to be observed at each stage of the synthesis process. The elemental composition of each sample is presented in Fig. S3.

The initial phase of MAX (Ti_3AlC_2) demonstrates a dense multilayer structure with well-defined grain boundaries and flat lamellar surfaces, which is typical for this class of nanolaminated materials.[30] After selective etching of aluminum to obtain MXene ($Ti_3C_2T_x$), a characteristic accordion-like morphol-ogy with an increased interlayer distance is observed, which confirms the successful removal of Al atoms and the formation of a multilayer two-dimensional structure.[31,32] The surface of activated carbon has a pronounced macroporous and rough texture with a well-developed system of open pores, which provides a high specific surface area, which is an important property for facilitating ion transfer and charge storage.[33]

The image of the MXene/Si composite obtained using SEM shows a uniform distribution of silicon nanoparticles over the surface of MXene. Small aggregation is observed in some areas, which is explained by interparticle interaction during synthesis.[25] The MXene/Si/AC triple composite demonstrates the most complex and heterogeneous morphology, where both silicon and activated carbon are embedded in an MXene layered matrix. It is expected that this structure will contribute to the formation of a conductive and ion-permeable network with high mechanical stability and effective buffering ability against bulk changes in silicon during cycling.[34,35] Thus, the obtained microstructures confirm the successful implementation of the concept of an integrated composite material combining high electrical conductivity, well-developed porosity and lithium storage capacity. These features make the synthesized structures promising candidates for use as anode materials in lithium-ion batteries.[36,37]

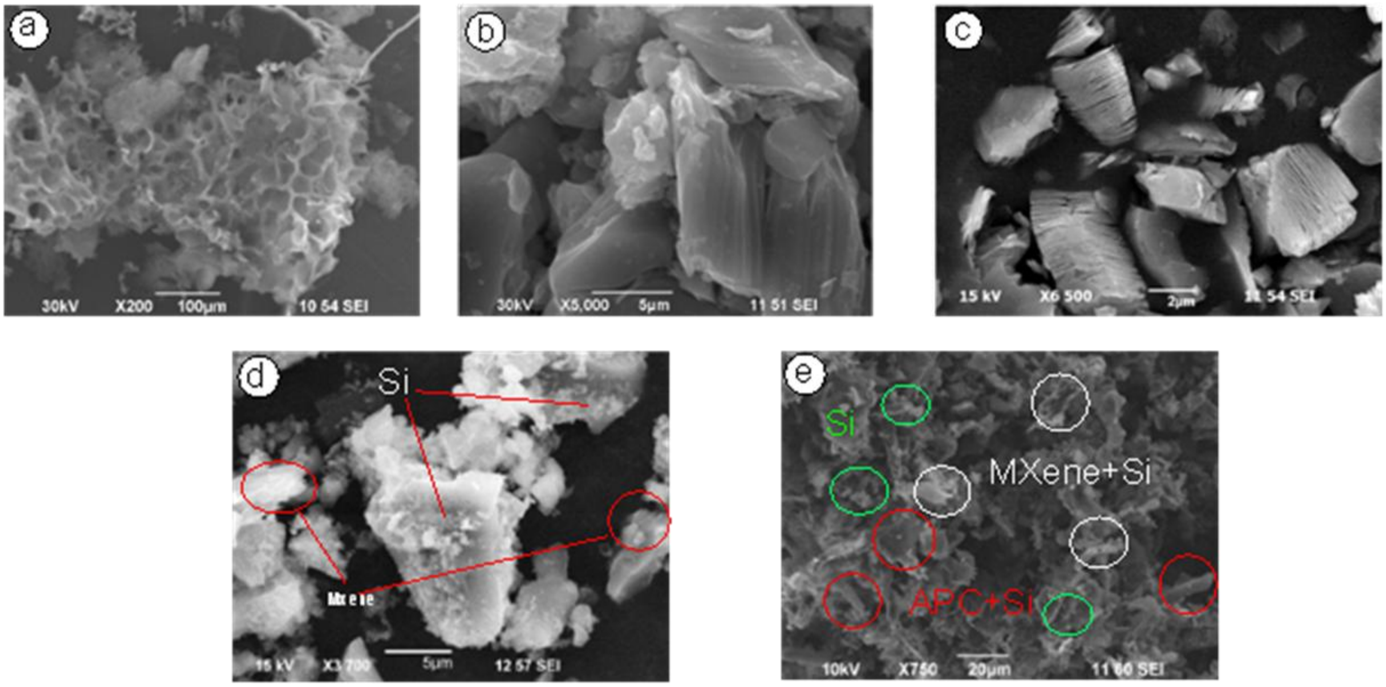

Fig. 7: SEM images: (a) Activated porous carbon, (b) MAX phase, c) Mxene, d) MXene/Si composite, e) AC/Si/MXene composite (after planetary ball mill).

Fig. 8 shows the X-ray diffraction patterns of individual components - activated carbon (AC), MXene ($Ti_3C_2T_x$), nanosilicon (Si), and the AC/Si/MXene composite. The AC diffraction pattern (below, red curve) shows broad and weak peaks centered around $2\theta \approx 25°$ and 44°, corresponding to the planes (002) and (100) of turbostrate or amorphous carbon.[38] This indicates the disordered nature and short - range structural order typical of activated carbon obtained from biomass precursors.[39] The MXene figure (blue curve) shows a strong peak (002) of about 2.7°, characteristic of $Ti_3C_2T_x$, along with a weaker reflection (004) of about 15°, confirming the successful etching of the MAX phase and the formation of a multilayer 2D structure.[31] The small-angle shift of peak (002) reflects the increased interlayer distance due to the presence of surface functional groups and ion intercalation.[32] Crystalline silicon (green curve) exhibits sharp, high-intensity peaks at $2\theta \approx 28.4°$, 47.3°, 56.1° and 69.1°, which correspond to the planes (111), (220), (311) and (400) cubic Si phase (JCPDS No. 27-1402).[40] The sharpness and intensity of the peak confirm the high crystallinity and phase purity of nanosilicon.

In the AC/Si/MXene composite (above, green curve), the

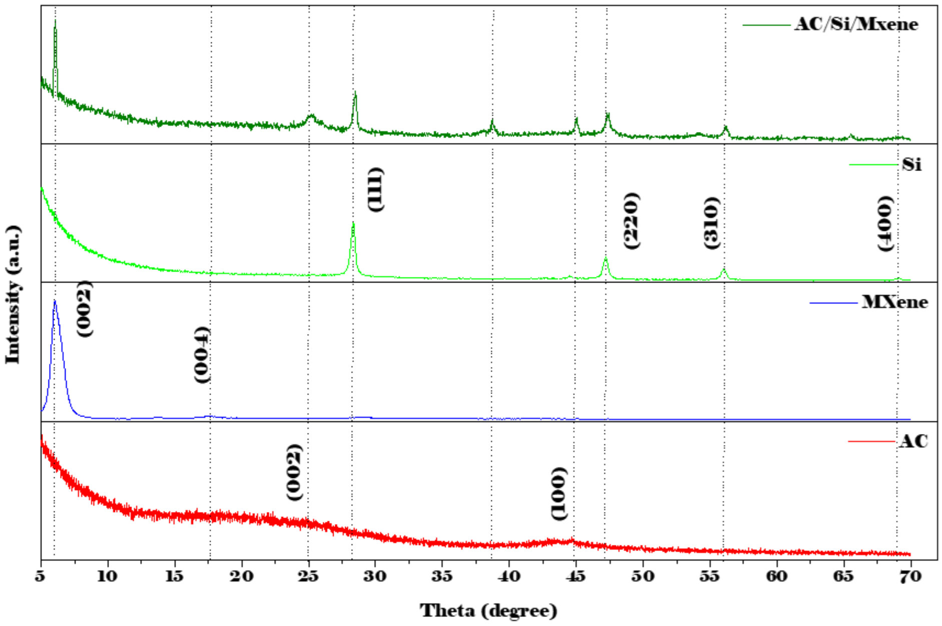

Fig. 8: XRD analysis of nanostructured silicon, MXene, and activated carbon.

diffraction pattern clearly includes the main peaks of crystalline silicon, the broadened amorphous background from AC, and the preserved low-angle (002) reflection from MXene. This confirms the structural integrity and successful integration of all components in the composite. The presence of separate phase signals without noticeable peak shifts implies minimal structural distortion during the manufacturing process.

Thus, the XRD results confirm the highly ordered crystal structure in the Nano-Si sample, the pronounced stacking of layers in MXene, and the amorphous nature of activated carbon, conclusions that are consistent with their morphological features and expected functional roles in lithium-ion energy storage systems. The electrochemical properties of the AC/Si/MXene composite electrode were evaluated using galvanostatic charge-discharge testing at various current densities. The results are shown in Fig. 9.

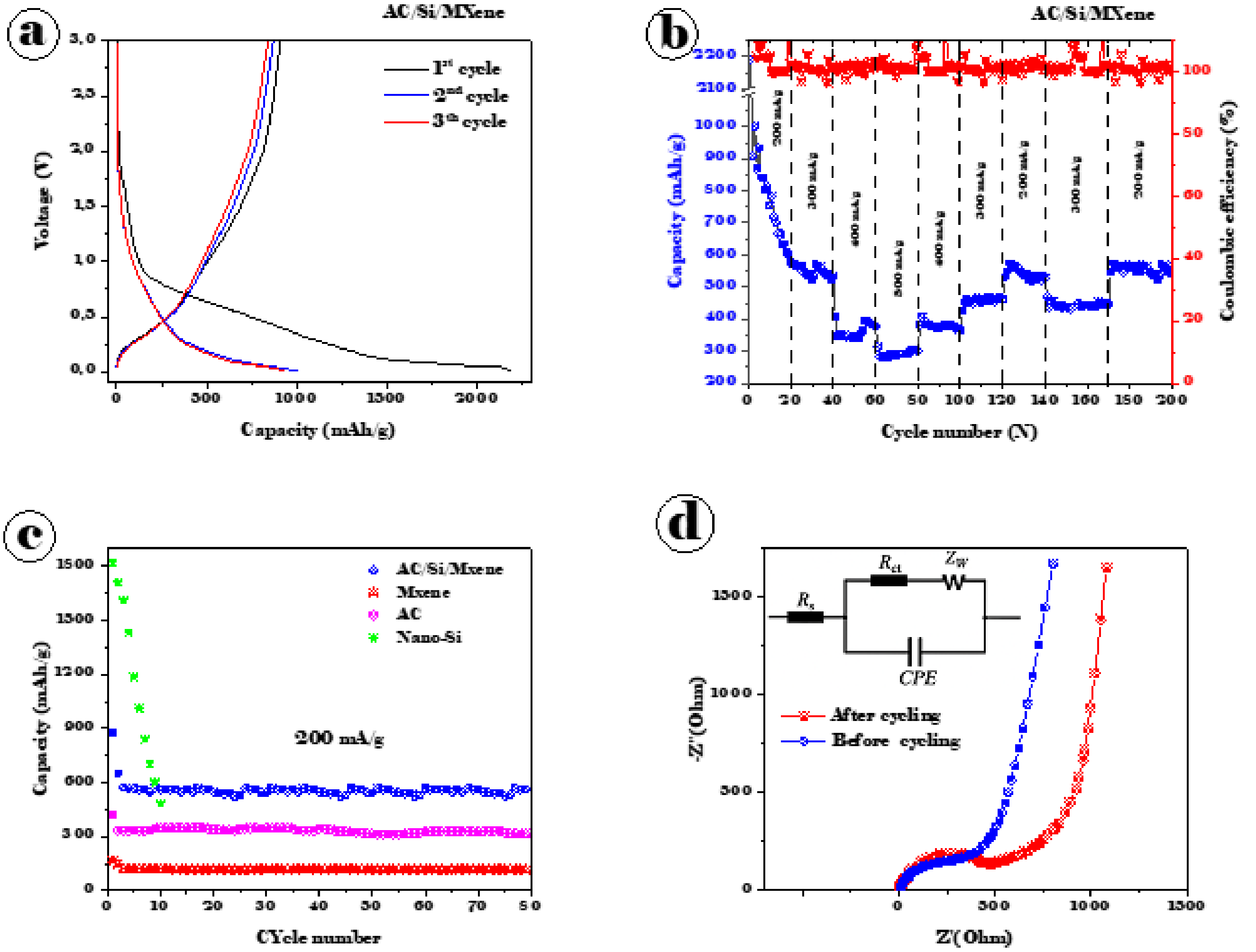

Fig. 9: Electrochemical performance of the AC/Si/MXene composite: (a) Charge–discharge voltage profiles; (b) Specific capacity as a function of current density; (c) Comparative analysis of cycling stability and capacity for individual components (AC, Si, MXene) and the composite; (d) Electrochemical impedance spectroscopy (EIS) Nyquist plot.

The cycling performance graph shows that the electrode provides a high initial specific capacity of approximately 2000 mAh/g at a low current density (200 mA/g) Fig. 9a. However, during the first 20 cycles, a significant drop in capacitance is observed, which is explained by irreversible processes such as the formation of a solid electrolyte interphase (SEI) and structural rearrangements of active components.[41-44] This composite, consisting of amorphous activated carbon, nanostructured silicon, and conductive MXene, is undergoing adaptive transformations aimed at stabilizing its mechanical and electronic integrity. These processes may include:

- redistribution of internal voltage due to volumetric changes in silicon during lithium/division;
- sealing of the electrode structure;
- stabilization of the SEI layer;
- improvement of the interfacial contact between the composite components, which leads to the formation of a strong conductive network.

After the initial decrease in capacity, there is a tendency to stabilize, indicating the establishment of a more stable composite architecture and the effectiveness of synergistic interactions between AC, Si and MXene components. When the current density changes (from 200 to 500 mA/g) Fig. 9b, the electrode retains a reasonable reversible capacity, demonstrating promising speed capability in high current conditions. In particular, upon returning to the initial current density (200 mA/g), capacitance is restored, which indicates a high structural integrity of the composite and favorable kinetic behavior for the intercalation of lithium ions Fig. 9c. Charge-discharge profiles (voltage versus capacitance) for the first three cycles show characteristic features typical of silicon-based anode materials. There is a marked difference between the first and subsequent cycles, primarily due to the initial formation of solid electrolyte interphase (SEI) and adverse reactions.[45] During the first discharge, a distinct plateau appears around ~0.2–0.3 V, which corresponds to silicon lithiation. When charging, characteristic plateaus are observed, indicating the process of division. The similarity of the profiles in the second and third cycles suggests a high degree of reversibility of the lithium/division reactions after initial stabilization.

Thus, galvanostatic analysis shows that the AC/Si/MXene electrode combines high specific capacity, good cycling characteristics, and stability at various current densities, making it a promising candidate for use in lithium-ion batteries.

To assess the contribution of each component to the overall electrochemical performance, separate tests were conducted for pure nanosilicon, activated carbon, and synthesized MXene at a current density of 200 mA/g (Fig. S1). Pure nanosilicon demonstrated a high initial specific capacity exceeding 1800 mAh/g in the first cycle. However, the material showed a significant decrease in capacity during cycling: by the 10th cycle, the capacity had dropped to about 400 mAh/g, and the test was subsequently discontinued due to instability. In contrast, activated carbon demonstrated stable performance, maintaining a specific capacity of about 300 mAh/g throughout the testing period. This stability is mainly due to its capacitive charge storage mechanism and the high structural strength of the material. The synthesized MXene also showed stable behavior: at a current density of 200 mA/g, it maintained a specific capacity of about 100 mAh/g for more than 80 cycles. This indicates the high electrochemical strength of MXene, despite its relatively low capacitance value. The speed characteristics of the individual components were not investigated in this study; however, theoretically, it can be assumed that at a current density of 200 mA/g, the composite material exhibits a higher specific capacity compared to each of the individual components. With a further increase in current density, a decrease in capacitance can also be expected for all materials, primarily due to limitations in the kinetics of lithium ion transport and increased polarization effects.

Fig. 9d shows a Nyquist graph illustrating the electrochemical impedance of an AC/Si/MXene composite anode. The experimental data are constructed as the imaginary and real parts of the complex impedance (Z'' and Z') in the frequency range from about 100 kHz to 3 Hz. In the high frequency region, there is a pronounced semicircle corresponding to the charge transfer resistance at the electrode–electrolyte interface. In the low frequency region, an elongated sloping tail is observed, characteristic of the Warburg impedance, which reflects the limitations of diffusion in the porous structure of the material. Fitting experimental data using the Rs+ equivalent circuit model (Rst||CP) + W gave the values of ohmic resistance Rs ≈ 9.6 Ohms and charge transfer resistance Rct ≈ 490 Ohms. The impedance spectra of each sample are shown separately in Fig. S2.

The first cycle (Fig. 10, black curve) shows clear differences from the subsequent ones, which is typical for silicon-based anode materials. This behavior is primarily explained by the formation of a solid electrolyte interfacial layer (SEI), accompanied by irreversible side reactions such as electrolyte decomposition and surface activation of silicon. A wide cathode plateau of about 0.2–0.3 V corresponds to the lithium of silicon and the formation of lithium-silicon alloys (for example, Li_xSi), while the anode plateau of about 0.5–0.6 V is associated with the process of division. Starting from the second cycle (red and blue curves), the CV profiles become highly stable and reproducible, indicating the formation of a stable SEI layer and a high degree of electrochemical reversibility. The preservation of the curve shape and the absence of significant peak shifts indicate the excellent structural integrity of the AC/Si/MXene composite and its effectiveness in adapting to bulk changes in silicon during cycling. Unlike individual components, the composite material, including nanosilicon, activated carbon, and MXene, demonstrated significantly higher and more stable capacity. For more than 80 cycles at a current density of 200 mA/g, the composite electrode retained a specific capacity of approximately 570-580 mAh/g. This performance indicates a synergistic effect between the components.: Activated carbon contributes to structural stability and electrical conductivity, MXene improves electron transfer, and nanosilicon provides high theoretical capacity.

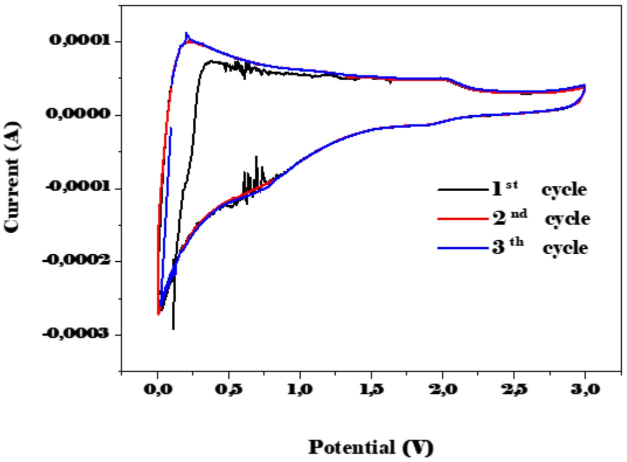

Fig. 10: Cyclic voltammetry (CV) curves of the AC/Si/MXene composite electrode recorded in the potential range of 0.01–3.0 V (vs. Li^+/Li) at a scan rate of 0.1 mV/s for the first three cycles.

Comparative analysis (Table 1 and Table S1) demonstrates that the proposed AC/Si/MXene composite exhibits one of the highest specific capacities among known MXene-based anodes for lithium-ion batteries. At a current density of 200 mA/g, this material provides a capacity of 580 mAh/g with a Coulombic efficiency of about 99%, which is superior to many previously published results. For example , Ti_3C_2TX

Table 1: Comparison of Capacity of MXene-Based Anode Materials in LIBs.

	Name	Capacity	Current density	CE	Year	Reference
1	AC/V_2C_D MXene	562 mAh/g	50 mA/g	95.87 %	2023	[45]
2	Ti_3C_2TX MXene-Encapsulated Silicon	550 mAh/g_t	1.7 A/g_t (0.5C)	~98%	2021	[46]
3	Bi_2MoO_6/MXene	328.2 mAh/g	at 2 A/g	99.6%	2019	[47]
4	Ti_2C MXene	389 mAh/g	100 mA/g	~99%	2016	[48]
5	Mn_2CT_x	764.7 mAh/g	0.5 C,	-	2024	[49]
6	Ti_2C	225 mAh/g	c/25	-	2012	[50]
7	Co-MOF/MXene	422 mAh/g	1 A/g	-	2024	[51]
8	Ti_3C_2Fx MXene	329 mA h/g	200 mA/g	-	2021	[52]
9	NTO@Mxene	207 mA h/g	0.1 A/g	~99%	2022	[53]
10	AC/Si/Mxene	580 mAh/g	200 mA/g	~99%		This work

MXene–Encapsulated Silicon demonstrated a capacity of 550 mAh/g at 0.5C (~98% CE),[46] while AC/V_2C_D MXene recorded a capacity of 562 mAh/g at 50 mA/g (95.87% CE).[45] It should be noted that even high-capacity materials such as Mn_2CT_x (764.7 mAh/g at 0.5C)[49] do not exhibit such stable Coulombic efficiency, and some other MXene composites (*e.g.*, Ti_2C or NTO@MXene) exhibit significantly lower capacity values (225 and 207 mAh/g, respectively).[50,53]

Thus, the synergistic effect between activated carbon, silicon, and MXene in the AC/Si/MXene structure provides an optimal combination of high capacity and stable process reversibility, making this material competitive with existing MXene-based anodes.

4. Conclusion

In this study, a hierarchical composite anode material based on activated carbon, nanoscale silicon, and MXene was successfully synthesized and characterized. Structural and morphological studies confirmed the formation of a well-dispersed porous architecture, while electrochemical testing revealed a high initial specific capacity (>2000 mAh/g) and stable cycling characteristics, with a reversible capacity of ~580 mAh/g after 80 cycles at a current density of 200 mA/g.

It should be especially noted that quantitative changes in the composition directly affect the electrochemical parameters. Pure nano-Si demonstrated a very high initial capacity (>1800 mAh/g), but quickly degraded to ~400 mAh/g within the first 10 cycles. Activated carbon had a lower capacity (~300 mAh/g) but high stability. MXene alone provided stability at ~100 mAh/g, acting as a conductive matrix. Unlike these individual components, the AC/Si/MXene composite combined their advantages, delivering a significant improvement in stability and reversible capacity. The synergistic effect is reflected in quantitative improvements: capacity retention at 570–580 mAh/g at 200 mA/g and a Coulombic efficiency of approximately 99%, surpassing many previously published results for MXene- or Si-based systems. This confirms that precise control of the component ratio and distribution is key to achieving an optimal balance between capacity, stability, and reversibility.

Overall, the developed AC/Si/MXene composite demonstrates high potential as a next-generation anode material for lithium-ion batteries, combining high capacity, improved cycling durability, and environmental friendliness thanks to the use of activated carbon from agricultural waste.

Acknowledgments

This research has been/was/is funded by the Science Committee of the Ministry of Science and Higher Education of the Republic of Kazakhstan (Grant No. AP19576865 and BR24992873).

Conflict of Interest

There is no conflict of interest.

Data availability

Data will be made available on request.

Supporting Information

Applicable.

CRediT Statement

Nadira Saitova: Writing – Original draft. **Kydyr Askaruly:** Methodology. **Nurlan Idrissov:** Data curation. **Zhanserik Kuli:** Investigation. **Kalizhan Shakenov:** Supervision. **Seitkhan Azat:** Writing – Review & editing. **Shynggyskhan Sultakhan:** Resources.

References

[1] N. Nasajpour-Esfahani, H. Garmestani, M. Bagheritabar, D. J. Jasim, D. Toghraie, S. Dadkhah, H. Firoozeh, Comprehensive review of lithium-ion battery materials and development challenges, *Renewable and Sustainable Energy Reviews*, 2024, **203**, 114783, doi: 10.1016/j.rser.2024.114783.

[2] M. Khan, Innovations in battery technology: enabling the revolution in electric vehicles and energy storage, *British Journal of Multidisciplinary and Advanced Studies*, 2024, **5**, 23-41, doi:

10.37745/bjmas.2022.0414.

[3] A. Yao, S. M. Benson, W. C. Chueh, Critically assessing sodium-ion technology roadmaps and scenarios for techno-economic competitiveness against lithium-ion batteries, *Nature Energy*, 2025, **10**, 404-416, doi: 10.1038/s41560-024-01701-9.

[4] H. Chen, Y. Xu, C. Liu, F. He, S. Hu, Storing energy in China: an overview, *Storing Energy*, Elsevier, Amsterdam, 2016, 509-527, doi: 10.1016/b978-0-12-803440-8.00024-5.

[5] J. Chen, K. Guo, T. Ren, G. Feng, W. Guo, F. Bao, Aluminium-doped vanadium nitride as cathode material for high-performance aqueous zinc-ion batteries, *Journal of Power Sources*, 2025, **626**, 235751, doi: 10.1016/j.jpowsour.2024.235751.

[6] R. Beissenov, A. Duisenbek, Y. Beisenova, K. Askaruly, M. Yeleuov, A. Abdisattar, Activated biomass-derived 3-dimensional porous graphene-like carbon for high-performance energy storage electrode materials, *Diamond and Related Materials*, 2024, **149**, 111588, doi: 10.1016/j.diamond.2024.111588.

[7] M. Nizam, H. Maghfiroh, A. Ubaidilah, I. Inayati, F. Adriyanto, Constant current-fuzzy logic algorithm for lithium-ion battery charging, *International Journal of Power Electronics and Drive Systems (IJPEDS)*, 2022, **13**, 926, doi: 10.11591/ijpeds.v13.i2.pp926-937.

[8] A. K. Mishra, Monika, B. S. Patial, A review on recent advances in anode materials in lithium ion batteries, *Materials Today Electronics*, 2024, **7**, 100089, doi: 10.1016/j.mtelec.2024.100089.

[9] F. Wang, B. Wang, J. Li, B. Wang, Y. Zhou, D. Wang, H. Liu, S. Dou, Prelithiation: a crucial strategy for boosting the practical application of next-generation lithium ion battery, *ACS Nano*, 2021, **15**, 2197-2218, doi: 10.1021/acsnano.0c10664.

[10] S. Chauque, F. Y. Oliva, A. Visintin, D. Barraco, E. P. M. Leiva, O. R. Cámara, Lithium titanate as anode material for lithium ion batteries: Synthesis, post-treatment and its electrochemical response, *Journal of Electroanalytical Chemistry*, 2017, **799**, 142-155, doi: 10.1016/j.jelechem.2017.05.052.

[11] K. Askaruly, S. Azat, X. Su, Amorphous SiO2/C as Anode for Lithium Ion Battery. In Innovative Materials for Environmental and Aerospace Applications; *IGI Global Scientific Publishing*, 2024, 113–136, doi: 10.4018/979-8-3373-0669-8.ch003.

[12] K. Askaruly, N. Idrissov, A. Abdisattar, S. Azat, Z. Kuli, M. Yeleuov, F. Malchik, C. Daulbayev, Y. Yszhan, B. Sarsembayeva, S. Nysanbayeva, Utilizing rice husk-derived Si/C composites to enhance energy capacity and cycle sustainability of lithium-ion batteries, *Diamond and Related Materials*, 2024, **149**, 111631, doi: 10.1016/j.diamond.2024.111631.

[13] C. E. L. Foss, M. K. Talkhoncheh, A. Ulvestad, H. F. Andersen, P. E. Vullum, N. P. Wagner, K. Friestad, A. Y. Koposov, A. van Duin, J. P. Mæhlen, Revisiting mechanism of silicon degradation in Li-ion batteries: effect of delithiation examined by microscopy combined with ReaxFF, *The Journal of Physical Chemistry Letters*, 2025, **16**, 2238-2244, doi: 10.1021/acs.jpclett.4c03620.

[14] E. Feyzi, A. K. M R, X. Li, S. Deng, J. Nanda, K. Zaghib, A comprehensive review of silicon anodes for high-energy lithium-ion batteries: Challenges, latest developments, and perspectives, *Next Energy*, 2024, **5**, 100176, doi: 10.1016/j.nxener.2024.100176.

[15] Q. Shi, J. Zhou, S. Ullah, X. Yang, K. Tokarska, B. Trzebicka, H. Q. Ta, M. H. Rümmeli, A review of recent developments in Si/C composite materials for Li-ion batteries, *Energy Storage Materials*, 2021, **34**, 735-754, doi: 10.1016/j.ensm.2020.10.026.

[16] Z. Zhang, Y. Wu, Z. Mo, X. Lei, X. Xie, X. Xue, H. Qin, H. Jiang, Research progress of silicon-based anode materials for lithium-ion batteries, *RSC Advances*, 2025, **15**, 10731-10753, doi: 10.1039/D5RA01268F.

[17] B. Jin, L. Liao, X. Shen, Z. Mei, Q. Du, L. Liang, B. Lei, J. Du, Advancement in research on silicon/carbon composite anode materials for lithium-ion batteries, *Metals*, 2025, **15**, 386, doi: 10.3390/met15040386.

[18] N.-S. Mussa, K. Askaruly, K. Bexeitova, S. Azat, K. Toshtay, Recent advancements in MXene-based catalysts: synthesis, characterization, and applications in sustainable energy production, *Carbon Trends*, 2025, **20**, 100551, doi: 10.1016/j.cartre.2025.100551.

[19] Y. Wu, P. Nie, J. Jiang, B. Ding, H. Dou, X. Zhang, MoS_2-nanosheet-decorated 2D titanium carbide (MXene) as high-performance anodes for sodium-ion batteries, *ChemElectroChem*, 2017, **4**, 1560-1565, doi: 10.1002/celc.201700060.

[20] H. Liu, X. Zhang, Y. Zhu, B. Cao, Q. Zhu, P. Zhang, B. Xu, F. Wu, R. Chen, Electrostatic self-assembly of 0D–2D SnO_2 quantum dots/$Ti_3C_2T_x$ MXene hybrids as anode for lithium-ion batteries, *Nano-Micro Letters*, 2019, **11**, 65, doi: 10.1007/s40820-019-0296-7.

[21] M. Jussambayev, K. Shakenov, S. Sultakhan, U. Zhantikeyev, K. Askaruly, K. Toshtay, S. Azat, MXenes for sustainable energy: a comprehensive review on conservation and storage applications, *Carbon Trends*, 2025, **19**, 100471, doi: 10.1016/j.cartre.2025.100471.

[22] X. Zhu, J. Shen, X. Chen, Y. Li, W. Peng, G. Zhang, F. Zhang, X. Fan, Enhanced cycling performance of Si-MXene nanohybrids as anode for high performance lithium ion batteries, *Chemical Engineering Journal*, 2019, **378**, 122212, doi: 10.1016/j.cej.2019.122212.

[23] X. Han, W. Zhou, M. Chen, J. Chen, G. Wang, B. Liu, L. Luo, S. Chen, Q. Zhang, S. Shi, C.-P. Wong, Interfacial nitrogen engineering of robust silicon/MXene anode toward high energy solid-state lithium-ion batteries, *Journal of Energy Chemistry*, 2022, **67**, 727-735, doi: 10.1016/j.jechem.2021.11.021.

[24] M. Xia, B. Chen, F. Gu, L. Zu, M. Xu, Y. Feng, Z. Wang, H. Zhang, C. Zhang, J. Yang, $Ti_3C_2T_x$ MXene nanosheets as a robust and conductive tight on Si anodes significantly enhance electrochemical lithium storage performance, *ACS Nano*, 2020, **14**, 5111-5120, doi: 10.1021/acsnano.0c01976.

[25] M. N. U. Chy, M. A. Rahman, J.-H. Kim, N. Barua, W. Abu Dujana, MXene as promising anode material for high-performance lithium-ion batteries: a comprehensive review, *Nanomaterials*, 2024, **14**, 616, doi: 10.3390/nano14070616.

[26] D. Seo, M.-R. Kim, J. Kyu Song, E. Kim, J. Koo, K.-C. Kim,

H. Han, Y. Lee, C. Won Ahn, Hollow Ti_3C_2 MXene/carbon nanofibers as an advanced anode material for lithium-ion batteries, *ChemElectroChem*, 2022, **9**, e202101344, doi: 10.1002/celc.202101344.

[27] L. Yu, L. Hu, B. Anasori, Y.-T. Liu, Q. Zhu, P. Zhang, Y. Gogotsi, B. Xu, MXene-bonded activated carbon as a flexible electrode for high-performance supercapacitors, *ACS Energy Letters*, 2018, **3**, 1597-1603, doi: 10.1021/acsenergylett.8b00718.

[28] M. Thommes, K. Kaneko, A. V. Neimark, J. P. Olivier, F. Rodriguez-Reinoso, J. Rouquerol, K. S. W. Sing, Physisorption of gases, with special reference to the evaluation of surface area and pore size distribution (IUPAC Technical Report), *Pure and Applied Chemistry*, 2015, **87**, 1051-1069, doi: 10.1515/pac-2014-1117.

[29] Y. Nishi and M. Inagaki, Gas Adsorption/Desorption Isotherm for Pore Structure Characterization, *Materials Science and Engineering of Carbon*, Butterworth-Heinemann, 2016, 227-247, ISBN- 9780128052563.

[30] M. W. Barsoum, The MN+1AXN phases: a new class of solids, *Progress in Solid State Chemistry*, 2000, **28**, 201-281, doi: 10.1016/s0079-6786(00)00006-6.

[31] M. Naguib, M. Kurtoglu, V. Presser, J. Lu, J. Niu, M. Heon, L. Hultman, Y. Gogotsi, M. W. Barsoum, Two-dimensional nanocrystals produced by exfoliation of Ti_3AlC_2, *Advanced Materials*, 2011, **23**, 4248-4253, doi: 10.1002/adma.201102306.

[32] B. Anasori, M. R. Lukatskaya, Y. Gogotsi, 2D metal carbides and nitrides (MXenes) for energy storage, *Nature Reviews Materials*, 2017, **2**, 16098, doi: 10.1038/natrevmats.2016.98.

[33] M. Sevilla, A. B. Fuertes, Sustainable porous carbons with a superior performance for CO_2 capture, *Energy & Environmental Science*, 2011, **4**, 1765, doi: 10.1039/c0ee00784f.

[34] X. Jiang, C. Tang, X. Zhou, J. Hou, S. Jiang, L. Meng, Y. Zhang, Recent progress in Si/$Ti_3C_2T_x$ MXene anode materials for lithium-ion batteries, *iScience*, 2024, **27**, 111217, doi: 10.1016/j.isci.2024.111217.

[35] M.-Q. Zhao, C. E. Ren, Z. Ling, M. R. Lukatskaya, C. Zhang, K. L. Van Aken, M. W. Barsoum, Y. Gogotsi, Flexible MXene/carbon nanotube composite paper with high volumetric capacitance, *Advanced Materials*, 2015, **27**, 339-345, doi: 10.1002/adma.201404140.

[36] D. Lin, Z. Lu, P.-C. Hsu, H. R. Lee, N. Liu, J. Zhao, H. Wang, C. Liu, Y. Cui, A high tap density secondary silicon particle anode fabricated by scalable mechanical pressing for lithium-ion batteries, *Energy & Environmental Science*, 2015, **8**, 2371-2376, doi: 10.1039/C5EE01363A.

[37] L. Wang, J. Yu, S. Li, F. Xi, W. Ma, K. Wei, J. Lu, Z. Tong, B. Liu, B. Luo, Recent advances in interface engineering of silicon anodes for enhanced lithium-ion battery performance, *Energy Storage Materials*, 2024, **66**, 103243, doi: 10.1016/j.ensm.2024.103243.

[38] H. Marsh, F. Rodríguez-Reinoso, Activated carbon (origins), *Activated Carbon*, Elsevier, Amsterdam, 2006, 13-86, doi: 10.1016/b978-008044463-5/50016-9.

[39] G. A. K. M. R. Bari, J.-H. Jeong, Porous carbon for CO_2 capture technology: unveiling fundamentals and innovations, *Surfaces*, 2023, **6**, 316-340, doi: 10.3390/surfaces6030023.

[40] D. ZhiLi, Fundamentals of Crystallography, Powder X-Ray Diffraction, and Transmission Electron Microscopy for Materials Scientists, *advances in materials science and engineering*, CRC Press, 2022, ISBN-978-0-429-35166-2.

[41] P. Zhang, D. Wang, Q. Zhu, N. Sun, F. Fu, B. Xu, Plate-to-layer Bi_2MoO_6/MXene-heterostructured anode for lithium-ion batteries, *Nano-Micro Letters*, 2019, **11**, 81, doi: 10.1007/s40820-019-0312-y.

[42] X. Han, W. Zhou, M. Chen, J. Chen, G. Wang, B. Liu, L. Luo, S. Chen, Q. Zhang, S. Shi, C.-P. Wong, Interfacial nitrogen engineering of robust silicon/MXene anode toward high energy solid-state lithium-ion batteries, *Journal of Energy Chemistry*, 2022, **67**, 727-735, doi: 10.1016/j.jechem.2021.11.021.

[43] N. P. Shetti, A. Mishra, S. Basu, T. M. Aminabhavi, A. Alodhayb, S. Pandiaraj, MXenes as Li-ion battery electrodes: progress and outlook, *Energy & Fuels*, 2023, **37**, 12541-12557, doi: 10.1021/acs.energyfuels.3c01346.

[44] X. Duan, C. Wang, F. Lv, T. Liu, X. Liu, Q. Wang, S. Yuan, Design and study N-doped 3D hollow sphere MXene with different nano curvatures as anodes for high-performance lithium-ion capacitors, *Electrochimica Acta*, 2025, **512**, 145510, doi: 10.1016/j.electacta.2024.145510.

[45] F. N. M. Azlan, M. A. A. M. Abdah, Y. S. Tan, M. N. Mustafa, R. Walvekar, M. Khalid, Microwave-etched V2C MXene-activated carbon hybrid as a high-performance anode material for lithium-ion batteries, *Journal of Energy Storage*, 2023, **72**, 108620, doi: 10.1016/j.est.2023.108620.

[46] K. Sarang, X. Zhao, D. Holta, H. Cao, K. Arole, P. Flouda, E.-S. Oh, M. Radovic, M. J. Green, J. L. Lutkenhaus, Carbon additive-free crumpled $Ti_3C_2T_X$ MXene-encapsulated silicon nanoparticle anodes for lithium-ion batteries, *ACS Applied Energy Materials*, 2021, **4**, 10762-10773, doi: 10.1021/acsaem.1c01736.

[47] P. Zhang, D. Wang, Q. Zhu, N. Sun, F. Fu, B. Xu, Plate-to-layer Bi_2MoO_6/MXene-heterostructured anode for lithium-ion batteries, *Nano-Micro Letters*, 2019, **11**, 81, doi: 10.1007/s40820-019-0312-y.

[48] B. Ahmed, D. H. Anjum, M. N. Hedhili, Y. Gogotsi, H. N. Alshareef, H_2O_2 assisted room temperature oxidation of Ti_2C MXene for Li-ion battery anodes, *Nanoscale*, 2016, **8**, 7580-7587, doi: 10.1039/c6nr00002a.

[49] Y. Wu, D. Liu, X. Wang, U. Ghani, M. A. Mushtaq, J. Yang, H. Sun, P. Tsiakaras, X. Cai, Mn-based MXene with high lithium-ion storage capacity, *Nano Research*, 2024, **17**, 4181-4191, doi: 10.1007/s12274-023-6360-0.

[50] M. Naguib, J. Come, B. Dyatkin, V. Presser, P.-L. Taberna, P. Simon, M. W. Barsoum, Y. Gogotsi, MXene: a promising transition metal carbide anode for lithium-ion batteries, *Electrochemistry Communications*, 2012, **16**, 61-64, doi: 10.1016/j.elecom.2012.01.002.

[51] Y. Chen, J. Cheng, A. Wang, C. Liu, H. Yan, Y. Qiu, Z. Wang, P. K. Chu, Y. Luo, The enhanced performance of Li-ion batteries based on Co-MOF/MXene composites, *Inorganic Chemistry Communications*, 2024, **159**, 111793, doi:

10.1016/j.inoche.2023.111793.

[52] T. Yin, Y. Li, R. Wang, O. A. Al-Hartomy, A. Al-Ghamdi, S. Wageh, X. Luo, X. Tang, H. Zhang, Synthesis of Ti3C2Fx MXene with controllable fluorination by electrochemical etching for lithium-ion batteries applications, *Ceramics International*, 2021, **47**, 28642-28649, doi: 10.1016/j.ceramint.2021.07.023.

[53] Y. Luo, Y. Zhao, J. Ma, Y. Huang, S. Han, M. Zhou, H. Lin, Sandwich-like $Na_2Ti_3O_7$ nanosheet/Ti_3C_2 MXene composite for high-performance lithium/sodium-ion batteries, *The Journal of Physical Chemistry C*, 2022, **126**, 18229-18237, doi: 10.1021/acs.jpcc.2c05670.

Open Access